arXiv:1506.00594v1 [cond-mat.soft] 1 Jun 2015

Nucleation of registered domains in the coupled leaflets of a bilayer

J. J. Williamson[1,*] and P. D. Olmsted[1,†]

[1] *Department of Physics, Institute for Soft Matter Synthesis and Metrology, Georgetown University, 37th and O Streets, N.W., Washington, D.C. 20057, USA*

(Dated: April 15, 2019)

We model the kinetics governing inter-leaflet domain registration (R) in a phase-separating bilayer. Theory and simulation show that hydrophobic mismatch can induce an instability towards a metastable antiregistered (AR) state upon quenching from high temperature. This necessitates a nucleation step to form the conventional registered bilayer phases. We then model the energetics for registered domains to nucleate from this metastable AR state, and find that an interplay between hydrophobic mismatch and thickness stretching/compression causes the effective hydrophobic mismatch to depend on domain size, which leads to strong departure from classical nucleation theory. We speculate on the implications for cell membrane rafts or clusters, whose size may be of similar magnitude to estimated critical radii for domain registration.

I. INTRODUCTION

A phase-separating amphiphilic bilayer may access competing equilibrium and metastable phase coexistences [1, 2] due to the presence of two coupled leaflets. A "direct" inter-leaflet coupling [3–7] promotes registered (R) bilayer phases in which both leaflets are enriched in the same species or ordering type (e.g. saturated lipid or liquid-ordered L_o). An "indirect" coupling from hydrophobic mismatch [8–10] promotes antiregistered (AR) phases, minimising variations in the bilayer thickness.

Depending on the choice of overall leaflet compositions, two (e.g. R-R) or three (e.g. R-R-AR [6]) bilayer phases may coexist. Using a lattice model of coupled leaflets that includes hydrophobic mismatch, we have shown that AR phases, though typically metastable, can be kinetically preferred [1], leading to kinetics in which a quenched bilayer passes through metastable states before equilibrating [2] – an example of Ostwald's "rule of stages" [11]. As well as presenting novel statistical thermodynamics whose understanding will allow greater control over artificial membranes, the underlying interactions could play a role in cell membrane rafts or clusters.

Immediately after quenching a bilayer to a phase-separating region, any spinodal instabilities to which the uniform state is subject compete to determine the dominant initial demixing mode. A bilayer with equimolar composition in each leaflet [12] can be subject to an "R mode" of symmetric composition perturbations between leaflets, and a perpendicular AR mode with asymmetric perturbations (Fig. 1) [1]. If the AR mode is fastest-growing, spinodal decomposition to AR-AR coexistence occurs first.

To equilibrate from a metastable AR-AR state, the bilayer must undergo nucleation of registered domains [2]. If nucleation is prohibitive, the bilayer can remain trapped in a metastable state. Hence, three classes of kinetics arise: direct separation into equilibrium phases, equilibration via nucleation out of a metastable state, or trapping in a metastable state. For other overall compositions, the picture becomes more complex, but the competition of AR and R phases and of metastable versus equilibrium states is qualitatively similar [2].

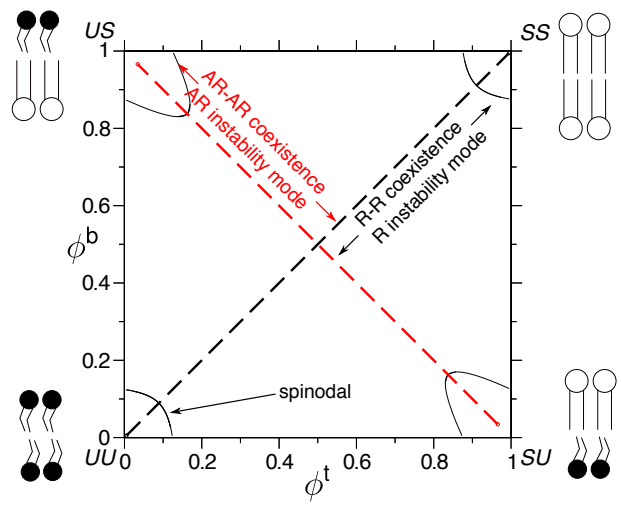

FIG. 1. Schematic phase diagram showing R-R and AR-AR central tie-lines available to a bilayer in which each leaflet has an overall equal area fractions mixture of species $(0.5, 0.5)$ and parameters such that both R and AR minima exist in the free-energy landscape [1]. Spinodals enclose the regions of local stability. Cartoons of the inter-leaflet arrangement in each phase are shown. Phase coexistences not considered in the present work are omitted [2]. Parameters: $\Delta_0 = 2\,a$, $\kappa = 3\,a^{-2}k_{\rm B}T$, $V = 0.6\,k_{\rm B}T$, $J = 4\,a^{-2}k_{\rm B}T$, $B = 0.48\,a^{-2}k_{\rm B}T$.

In this paper, we examine the nucleation energetics that determine whether equilibrium is reached from a metastable state. After first identifying the three classes of kinetics in simulation, guided by an instability analysis [1], we develop a theory for the nucleation of registered domains, which captures the interplay of bulk free energy with thickness mismatch at the domain perimeter. The predicted nucleation barriers and critical radii are

* johnjosephwilliamson@gmail.com
† pdo7@georgetown.edu

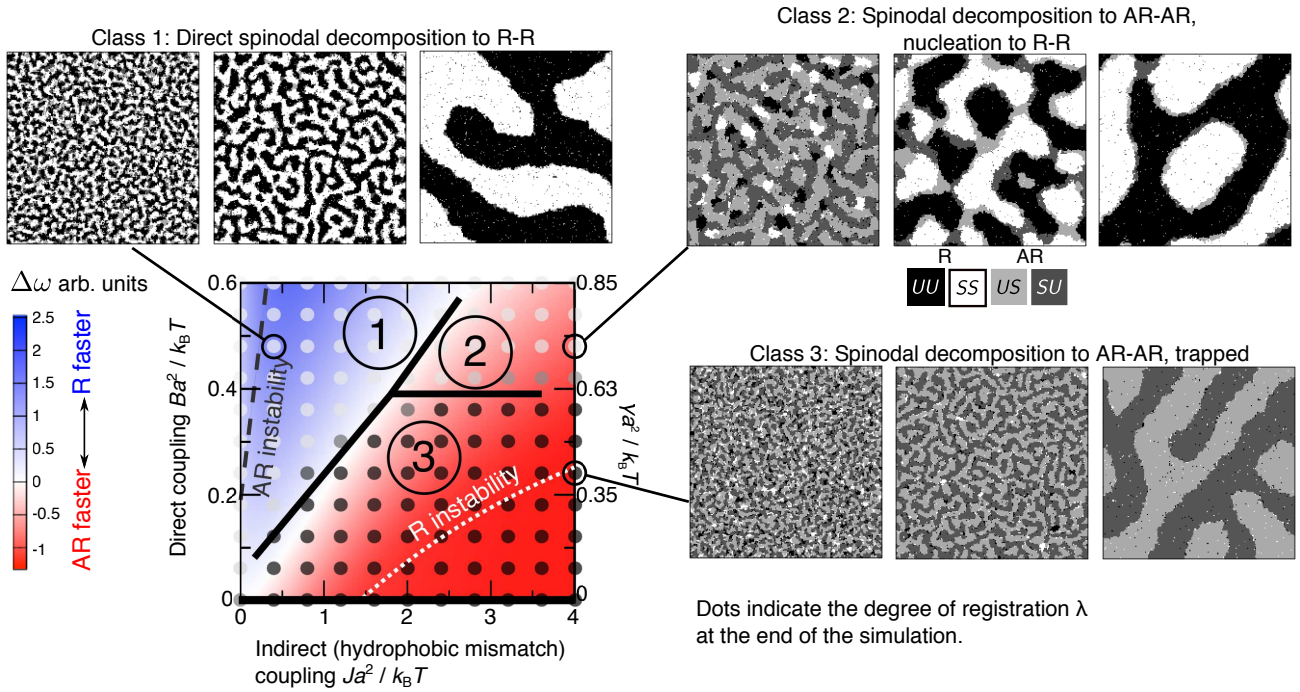

FIG. 2. Mean-field parameter map showing the relative growth rates (blue/red) of R and AR instability modes for a $(0.5, 0.5)$ bilayer from linear stability analysis of initial demixing [1], with $\Delta_0 = 2\,a$, $\kappa = 3\,a^{-2} k_{\rm B}T$, $V = 0.6\,k_{\rm B}T$. The equilibrium state is R-R in all cases. Overlaid dots from simulation (with $V = 0.9\,k_{\rm B}T$) show the average degree of registration λ at the end of the simulation time, $\lambda = 0$ (black) to $\lambda = 1$ (white). Three distinct classes of kinetics are identified, with illustrative snapshot sequences ($\mathcal{L}=200$ in the snapshots). Below the "AR instability" line AR-AR coexistence is possible but is metastable. Below the "R instability" line the homogeneous state is no longer unstable to R phase separation, although R-R is still the equilibrium state. Simulations are visualised with OVITO [13].

consistent with our simulation results. We find that the effective hydrophobic mismatch between a domain and its surroundings is domain size-dependent, which causes strong departure from classical nucleation theory.

II. MODEL

A. Lattice model

A detailed description of our model appears in [1, 2]. A local bilayer patch is described as N lattice sites with top and bottom-leaflet amphiphiles. The amphiphiles' hydrophobic lengths $\ell_i^{\rm t(b)}$ lead to the bilayer thickness $d_i \equiv \ell_i^{\rm t} + \ell_i^{\rm b}$ and difference $\Delta_i \equiv \ell_i^{\rm t} - \ell_i^{\rm b}$. Model species S and U represent saturated and unsaturated lipid species or, e.g., the liquid-ordered (L_o) and liquid-disordered (L_d) lipid phases in the two phase region of a ternary mixture [2].

The Hamiltonian is

$$H = \sum_{<i,j>} (V_{\hat{\phi}_i^{\rm t}\hat{\phi}_j^{\rm t}} + V_{\hat{\phi}_i^{\rm b}\hat{\phi}_j^{\rm b}}) + \sum_{<i,j>} \tfrac{1}{2}\tilde{J}(d_i - d_j)^2 + \sum_i \tfrac{1}{2}B(\Delta_i)^2 + \sum_i \tfrac{1}{2}\kappa\left((\ell_i^{\rm t} - \ell_0^{{\rm t}i})^2 + (\ell_i^{\rm b} - \ell_0^{{\rm b}i})^2\right) , \quad (1)$$

where $\hat{\phi}_i^{\rm t(b)} = 1$ if the top (bottom) of site i contains an S amphiphile, $\hat{\phi}_i^{\rm t(b)} = 0$ if U. The species-dependent ideal hydrophobic lengths are $\ell_0^{{\rm t(b)}i} = \ell_{S0}$ for an S amphiphile at the top (bottom) of site i, or ℓ_{U0} for U, and each site is pairwise registered (SS or UU) or antiregistered (SU or US).

$V \equiv V_{10} - \frac{1}{2}(V_{00} + V_{11})$ quantifies intra-leaflet interactions independent of length, such as those between headgroups. The "direct" coupling B promotes registration by minimising length mismatch (hence implicitly tail structure mismatch [1, 14]) across the midplane. It can be related to the conventional inter-leaflet mismatch energy γ [1] which is shown on Fig. 2 as well. The hydrophobic "indirect" coupling $\tilde{J}$ promotes antiregistration by penalising mismatch in the bilayer thickness profile. We also define $J \equiv 4\tilde{J}$, which appears in the mean-field approximation of Eq. 1 [1]. κ can be related to the area compression modulus κ_A, and penalises variation from species-dependent ideal length. Hence, the mismatch $\Delta_0 \equiv \ell_{S0} - \ell_{U0}$ couples to the length-dependent interactions J and B to determine the strength of indirect and direct coupling between the species (we choose $\ell_{S0} > \ell_{U0}$ although this is arbitrary). The reference total thickness $d_0 \equiv \ell_{S0} + \ell_{U0}$ is irrelevant to the model behaviour in the absence of an external field acting on

bilayer thickness.

B. Protocol

We simulate a $\mathcal{L}^2 = \mathcal{N}$ bilayer where $\mathcal{L} = 100$ (where script letters refer to the entire simulated bilayer, as opposed to a local bilayer patch). The Kinetic Monte Carlo scheme is as described in [2]. The overall leaflet compositions are conserved (since we do not consider flip-flop or exchange with the solvent), and are given by

$$\Phi^{\mathrm{t(b)}} \equiv \frac{\mathcal{N}_S^{\mathrm{t(b)}}}{\mathcal{N}} \ . \tag{2}$$

R and AR lattice sites can interconvert ($SU + US \rightleftarrows SS + UU$) to alter the degree of registration

$$\lambda \equiv \frac{\mathcal{N}_{SS} + \mathcal{N}_{UU}}{\mathcal{N}} \ , \tag{3}$$

which can vary in the range

$$1 - |\Phi^{\mathrm{t}} - \Phi^{\mathrm{b}}| \leq \lambda \leq |\Phi^{\mathrm{t}} + \Phi^{\mathrm{b}} - 1| \ . \tag{4}$$

Changes in λ can be used to monitor transitions between states that differ in their amount of registered and antiregistered phases [2].

C. Parameters

The lattice spacing is $a \sim 0.8\,\mathrm{nm}$ [1]. As in [2] we use $\kappa = 3\,a^{-2} k_{\mathrm{B}} T$, corresponding to $\kappa_A \approx 60\,k_{\mathrm{B}} T \mathrm{nm}^{-2}$, in the range for lipid bilayers at 300 K [15–17]. We choose a length mismatch $\Delta_0 = 2\,a \sim 1.5\,\mathrm{nm}$, somewhat larger than in typical phospholipid mixtures, for which phase height mismatch $\lesssim 2\,\mathrm{nm}$ [18, 19] would imply $\Delta_0 \lesssim 1\,\mathrm{nm}$. A large Δ_0 couples to both the indirect (J) and direct (B) couplings, thus increasing the energetic driving forces for both antiregistration and registration and making the competing phases clearer to interpret; the phenomenology is qualitatively similar upon reducing Δ_0 [2]. We use $V = 0.6\,k_{\mathrm{B}} T$ in our mean-field theory theory, above the mean-field threshold $V_0 \equiv 0.5\,k_{\mathrm{B}} T$ for phase separation in the absence of other couplings, and use $V = 0.9\,k_{\mathrm{B}} T$ in simulation, where the corresponding threshold is $V_0^{\mathrm{sim.}} = 0.88\,k_{\mathrm{B}} T$ due to fluctuations [20]. Although we cannot expect precise quantitative agreement between the mean-field theory and simulation, in this regime it appears the exact value of V is not too important to the kinetics; changing to $V = 0.9\,k_{\mathrm{B}} T$ does not strongly affect the theoretical relative R/AR growth rate $\Delta\omega$ calculated in Fig. 2 [2].

Here we only consider overall composition $\Phi^{\mathrm{t}} = \Phi^{\mathrm{b}} = 0.5$, denoted $(0.5, 0.5)$. By Eq. 4 the degree of registration λ can vary from 0 (full antiregistration) to 1 (full registration). $\lambda \approx 0$ identifies AR-AR coexistence, while $\lambda \approx 1$ identifies R-R. Other overall compositions yield different states including three-phase coexistence (AR-AR-R or R-R-AR) while retaining the qualitative kinetics of metastable versus equilibrium states [2].

D. Competing states and initial demixing

Eq. 1 yields a mean-field free energy f which can be used to calculate phase coexistence in the space of locally-averaged compositions $\phi^{\mathrm{t(b)}} \equiv N_S^{\mathrm{t(b)}}/N$ [1]. Fig. 1 schematically shows the competing R-R and AR-AR phase coexistences relevant to the present work; further details can be found in [1, 2]. Linear stability analysis of the initial homogeneous state yields the relative growth rates of competing R versus AR instability modes [1].

In Fig. 2, R-R separation is equilibrium (except for a very small region $Ba^2/k_{\mathrm{B}}T \lesssim 0.005$). Below the "AR instability" line, AR-AR separation is also possible so can compete with R-R. Below the "R instability" line the initial state is not subject to R instability although R-R separation remains the equilibrium state. The red and blue colours show the relative growth rates of R and AR instability modes, with the difference $\Delta\omega$ determining which mode dominates the initial demixing.

III. KINETIC PHASE DIAGRAM

Fig. 2 shows the simulation results for varying indirect coupling J and direct coupling B. The simulations map out whether registered or antiregistered domains dominate at the end of the simulated time (10^6 Monte Carlo Steps) by measuring the degree of registration λ. Since we use $(0.5, 0.5)$ overall composition, $\lambda \approx 0$ corresponds to AR-AR coexistence, and $\lambda \approx 1$ to R-R. Each dot on Fig. 2 is an average of four independent trajectories.

This simulated "kinetic phase diagram" agrees semi-quantitively with the theoretical linear stability analysis of initial demixing (red/blue on Fig. 2) in that inside the blue region, where R-R coexistence should be accessed directly, the simulation exhibits full registration. If instead the AR mode is fastest (red), we find two possibilities; the bilayer may reach R-R coexistence by nucleation out of the AR-AR state, or remain metastably trapped in it. Fig. 3a shows the successful formation of registered nuclei, which grow from the boundaries of antiregistered domains. In Fig. 3b, a different random quench in the simulation leads to failure to nucleate despite unchanged parameters, illustrating the stochastic nature of the nucleation process.

Having identified the expected three classes of kinetics, we next model the nucleation energetics that govern nucleation of registered domains, hence clarifying the different possible fates of the metastable AR-AR state (the second and third kinetic classes identified in Fig. 2).

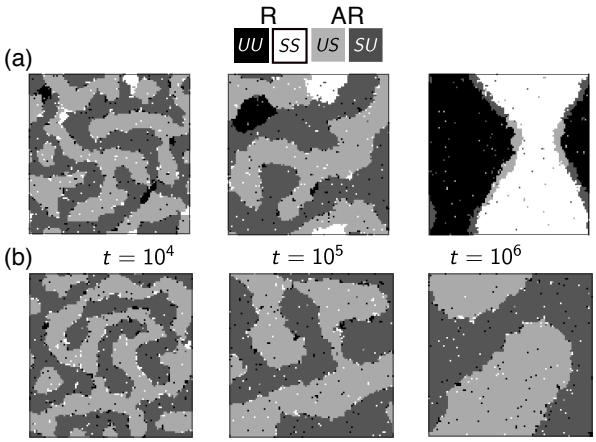

FIG. 3. (a) Snapshots showing a trajectory in which two successful registered nuclei grow to reach equilibrium. (b) Trajectory with the same parameters but a different random seed, in which no nuclei survive. Parameters: $\Delta_0 = 2\,a$, $\kappa = 3\,a^{-2}k_{\rm B}T$, $V = 0.6\,k_{\rm B}T$, $J = 4\,a^{-2}k_{\rm B}T$, $B = 0.42\,a^{-2}k_{\rm B}T$, $\mathcal{L} = 100$.

IV. NUCLEATION THEORY

The metastability of antiregistered phases implies that arbitrarily small composition fluctuations decay. Registered domains must therefore be formed by compositional fluctuations sufficient to generate a nucleus of a registered phase, which must be large enough for the area-dependent payoff in bulk free energy to outweigh the penalty for hydrophobic mismatch at the edge. We study the energetics of this nucleation. For simplicity we consider the R nucleus to be compositionally uniform (thus ignoring mixing effects at the domain boundary), and use the response of the thickness profile to mismatch at the nucleus' boundary to calculate the nucleation energetics.

Fig. 3a exhibits typical nucleation of registered domains. Our goal is to model the role of hydrophobic mismatch around the edge of R nuclei in determining whether they successfully grow (Fig. 3a) or decay (Fig. 3b). For the reference (zero free energy) state, we take a registered bilayer at equilibrium with no transmidplane mismatch and domains coarse enough for edges to make a vanishing energy contribution. We then assume that a dominant AR instability mode has lead to an initially antiregistered state, which incurs everywhere an energy cost, relative to the registered reference state, due to the direct coupling B. We then introduce a circular R nucleus of radius R, thus removing the direct coupling energy within the domain's area but introducing a thickness mismatch around its perimeter (Fig. 4).

In the continuum limit of the lattice model, the free energy is

$$G_{\rm cont} = \frac{1}{2}\int_0^\infty \frac{2\pi r dr}{a^2}\Bigg(\kappa\big(\ell^{\rm t}(r) - \ell_0^{\rm t}(r)\big)^2 + \kappa\big(\ell^{\rm b}(r) - \ell_0^{\rm b}(r)\big)^2 + \tilde{J}a^2\left(\frac{dd(r)}{dr}\right)^2 + B\big(\ell^{\rm t}(r) - \ell^{\rm b}(r)\big)^2\Bigg)\,, \tag{5}$$

where a is the lattice spacing and the $\tilde{J}$ term captures the corresponding neighbour interaction (Eq. 1) in the limit of small lattice spacing. We neglect contributions from the Ising-like interaction V which would depend on the precise shape of any pre-existing (AR) domain boundaries in the region *before* the R nucleus were introduced. When the R nucleus is introduced these boundaries are replaced by an R-AR boundary of similar length, leaving the Ising contribution approximately unchanged. Indeed, the results of Ref. [18] suggest that, as hydrophobic mismatch increases, it becomes the dominant contribution to the line tension of (registered) domains. It is important to note that this does not imply that thickness mismatch uniquely determines phase-transition temperature [21].

The leaflet compositions are reflected in the ideal thicknesses $\ell_0^{\rm t,b}(r)$. The actual thickness profiles $\ell^{\rm t,b}(r)$ adopted by the leaflets minimise the free energy $G_{\rm cont}$. The actual thickness difference and total thickness profiles are denoted $\Delta(r) \equiv \ell^{\rm t}(r) - \ell^{\rm b}(r)$ and $d(r) \equiv \ell^{\rm t}(r) + \ell^{\rm b}(r)$. The calculations underlying the following results are detailed in the Appendix.

A. Antiregistered background

Before the nucleus is introduced we have an AR background. For simplicity we assume strong compositional segregation so that the phases are approximately pure, with ideal leaflet thicknesses given by

$$\ell_0^{\rm t,\,AR} = \ell_{S0}\ , \tag{6a}$$

$$\ell_0^{\rm b,\,AR} = \ell_{U0}\ , \tag{6b}$$

where we have arbitrarily assumed S lipids in the top leaflet, U in the bottom (since we are ignoring the Ising contribution V the pattern and orientation of the antiregistered domains is unimportant). This yields

$$\Delta^{\rm AR} = \frac{\kappa\Delta_0}{\kappa + 2B}\ , \tag{7}$$

for the difference in actual leaflet thicknesses. The species in each leaflet adapt their tail lengths (hence degree of tail ordering [1, 14]) to one another's presence, balancing tail stretching with the direct coupling energy. Relaxing the assumption of strong compositional segregation would not qualitatively affect the physics. The physical content of Eq. 7 is simply that mismatched ideal lengths

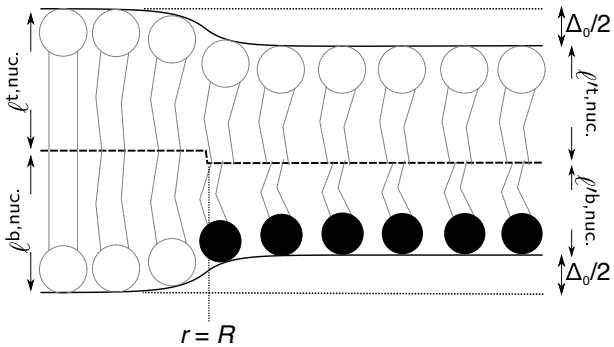

FIG. 4. Schematic structure of a registered nucleus introduced to an antiregistered background. The leaflet thicknesses inside and outside the nucleus are calculated from Eq. 15. The midplane (dashed line) shifts discontinuously at $r = R$ to maintain smooth outer contours (cf. [9]). S (light) and U (dark) amphiphiles illustrating composition are superimposed. Primes indicate that the leaflet thicknesses outside the nucleus differ from those inside.

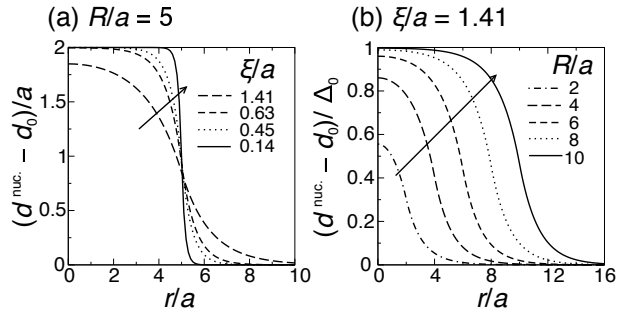

FIG. 5. (a) Calculated total thickness within the registered nucleus $d^{\text{nuc.}}(r)$ relative to the AR background. The *ideal* thickness of the nucleus relative to its surroundings is $\Delta_0 = 2\,a$. The arrow indicates decreasing decay length ξ. (b) $d^{\text{nuc.}}(r)$ relative to the AR background and normalised by its ideal value inside the nucleus, Δ_0, with the arrow indicating increasing nucleus size.

in an AR phase cause a free-energy cost; in strong compositional segregation this energy density is (see Eq. A5)

$$\gamma = \frac{\Delta_0^2 \kappa B}{2a^2(\kappa + 2B)} \ . \tag{8}$$

Since no mismatches in total ideal thickness exist, d^{AR} is uniform:

$$d^{\text{AR}} = \ell_{S0} + \ell_{U0} = d_0 \ . \tag{9}$$

B. Introducing a registered nucleus

For concreteness, we consider the energy change induced by a registered nucleus of the S species (Fig. 4), with larger ideal thickness than its surroundings (the energetics are identical for a nucleus of the shorter species U):

$$\ell_0^{\text{t, nuc.}}(r) = \ell_{S0} \ , \tag{10a}$$

$$\ell_0^{\text{b, nuc.}}(r) = \begin{cases} \ell_{S0} & \text{if } r \le R \\ \ell_{U0} & \text{if } r > R \ . \end{cases} \tag{10b}$$

The top and bottom leaflets have the same composition (ideal thickness) within the nucleus, removing the interleaflet mismatch within the region $r \le R$ and leading to an area-dependent free energy payoff via the B term of Eq. 5. The actual thickness difference profile is now

$$\Delta^{\text{nuc.}}(r) = \begin{cases} 0 & \text{if } r \le R \\ \dfrac{\kappa \Delta_0}{\kappa + 2B} & \text{if } r > R \ . \end{cases} \tag{11}$$

The discontinuity arises from the discontinuous composition at $r = R$ and the fact that, in contrast to the total thickness $d(r)$, no energy in the Hamiltonian penalises variation in the thickness *difference* $\Delta(r)$.

If the composition interface were not sharp one would consider the coupling between composition and thickness gradients. Moreover, one could also allow for sliding into antiregistration at a registered domain boundary, which smears out thickness mismatch [2, 9]. These would not qualitatively alter the fact that the registered nucleus' boundary experiences an energy cost from thickness mismatch.

Calculating the total thickness profile after the nucleus is introduced yields

$$d^{\text{nuc.}}(r) = d_0 + \begin{cases} \Delta_0 \left[1 - \frac{R}{\xi} K_1\left(\frac{R}{\xi}\right) I_0\left(\frac{r}{\xi}\right) \right] & \text{if } r \le R \\ \Delta_0 \left[\frac{R}{\xi} I_1\left(\frac{R}{\xi}\right) K_0\left(\frac{r}{\xi}\right) \right] & \text{if } r > R \ . \end{cases} \tag{12}$$

Here, I_n and K_n are nth order modified Bessel functions of the first and second kind respectively. Their spatial dependence is controlled by a decay length

$$\xi \equiv \sqrt{2\tilde{J}a^2/\kappa} \ , \tag{13}$$

which quantifies the competition between hydrophobicity and stretching. Eq. 12 shows how the mismatch in ideal total thickness at $r = R$ distorts the thickness profile both inside and outside the registered nucleus. The decay length ξ controls the lateral distance over which $d^{\text{nuc.}}(r)$ is perturbed (Fig. 5a).

For large ξ, the R nucleus does not reach its ideal thickness even at its centre, $r/a = 0$. This is an important point; for small nuclei $R \sim \xi$, the *effective* thickness mismatch between the nucleus and its surroundings is less than its value Δ_0 in the limit of large domain size (Fig. 5b). The thickness at the centre of the nucleus is given by

$$d^{\text{nuc.}}(0) = d_0 + \Delta_0 \left[1 - \frac{R}{\xi} K_1\left(\frac{R}{\xi}\right) \right] \ . \tag{14}$$

Hence, small domains have smaller hydrophobic mismatch so experience a smaller effective line tension. This dependence of domain height on domain size could be observed by atomic force microscopy. Since $\tilde{J}$ and κ will typically be of the same order of magnitude [1] such that $\xi \sim a$, it may only be significant for very small domains. However, increasing thickness mismatch of registered domains as they grow has been reported in molecular simulation [22], as predicted here.

After introducing the nucleus, the individual thicknesses $\ell^{\mathrm{t,\ nuc.}}(r)$ and $\ell^{\mathrm{b,\ nuc.}}(r)$ of the top and bottom leaflets are given by

$$\ell^{\mathrm{t,\ nuc.}}(r) = \tfrac{1}{2}\left(d^{\mathrm{nuc.}}(r) + \Delta^{\mathrm{nuc.}}(r)\right) \ , \tag{15a}$$

$$\ell^{\mathrm{b,\ nuc.}}(r) = \tfrac{1}{2}\left(d^{\mathrm{nuc.}}(r) - \Delta^{\mathrm{nuc.}}(r)\right) \ . \tag{15b}$$

Assuming no empty space inside the bilayer, the leaflet thicknesses fully determine the outer contours of the bilayer once the midplane position is specified. Noting that $\Delta^{\mathrm{nuc.}}(r)$ (thus $\ell^{\mathrm{t,\ nuc.}}(r)$ and $\ell^{\mathrm{b,\ nuc.}}(r)$) is discontinuous at the nucleus boundary $r = R$, we expect this discontinuity to occur in the midplane position to maintain smooth outer contours and minimise hydrophobic exposure. This can also be seen in molecular simulations containing AR domains [9]. The resultant bilayer structure is shown in Fig. 4. Outside the R nucleus, the leaflets adapt their thicknesses (thus tail ordering) to one another's presence (Eq. 11), i.e. the S species are shorter than ℓ_{S0} and the U longer than ℓ_{U0}. Inside the nucleus, the registered region is able to achieve its ideal thickness only once the nucleus grows large enough.

C. Energy of a registered nucleus

Given the thickness profiles before and after the nucleus is introduced, the energy required to create a registered nucleus of size R is given by

$$\Delta G = \frac{\Delta_0^2 \kappa}{2a^2}\pi R^2 \left(-\frac{B}{\kappa + 2B} + I_1\left(\tfrac{R}{\xi}\right) K_1\left(\tfrac{R}{\xi}\right)\right) \ . \tag{16}$$

The negative term $\propto R^2$ arises from the removal of inter-leaflet mismatch over the domain's area, and the positive term arises from hydrophobic mismatch. For large nucleus size R relative to the decay length ξ, the approximations $I_n(x) \sim \exp(x)/\sqrt{2\pi x}$ and $K_n(x) \sim \exp(-x)\sqrt{\pi/2x}$ for large x give $I_1(\frac{R}{\xi})K_1(\frac{R}{\xi}) \sim \xi/2R$. The hydrophobic mismatch term then becomes overall linear in R, acting like a standard line tension of magnitude $\Delta_0^2\kappa\xi/8a^2$. Hence, for large nuclei or large stiffness κ, ΔG will behave as in 2D classical nucleation theory (CNT).

Some illustrative nucleation energy curves are shown in Fig. 6. For CNT in 2D, the function $\Delta G/R$ would be a straight line of negative slope. Deviation from a straight line indicates deviation from CNT. If ξ is small (weak hydrophobicity compared to stiffness), the behaviour is CNT-like over most of R; moreover the critical radius R^* (defined as the value where $\Delta G(R)$ is maximised) occurs deep into the CNT-like regime. For larger ξ (stronger hydrophobicity relative to stiffness) the critical radius no longer occurs in the CNT-like regime, so non-CNT effects arising from nonlocal thickness deformation influence nucleation.

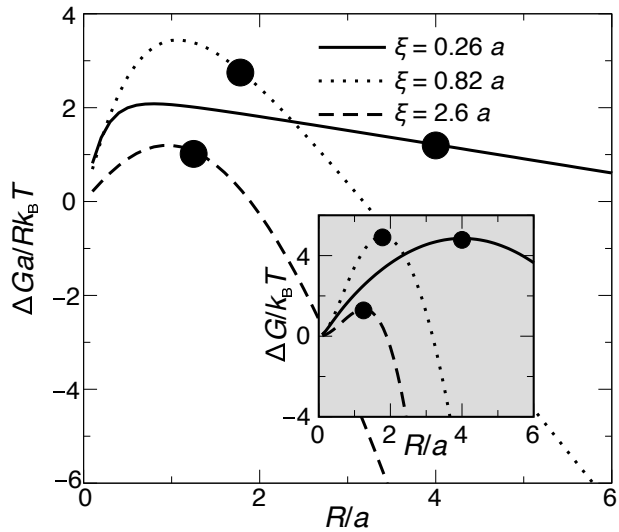

FIG. 6. Energy ΔG for a registered nucleus of radius R, calculated from Eq. 16, with difference in ideal species lengths is $\Delta_0 = 2\,a$ and stretch modulus $\kappa = 3\,a^{-2}k_{\mathrm{B}}T$. We vary the decay length ξ by varying $\tilde{J}$ while holding ratio of indirect and direct couplings constant at $\tilde{J}/B = 2$ ($J/B = 8$ line in Fig. 7). In 2D classical nucleation theory the product $\Delta Ga/R$ would yield a straight line of negative slope. Circles show locations of the critical radii R^*. Inset: behaviour of ΔG without normalisation by nucleus size.

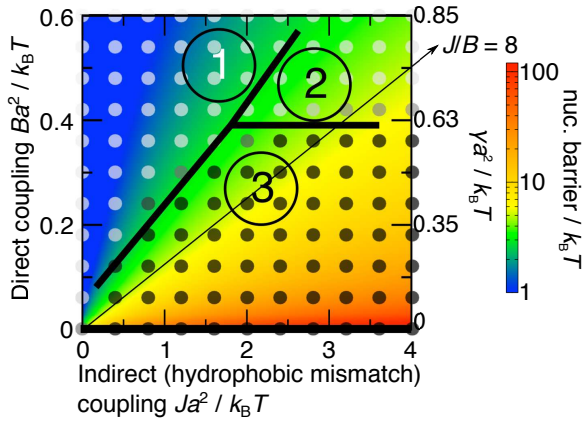

FIG. 7. Simulated kinetic phase diagram (notation as in Fig. 2), now overlaid on the theoretical nucleation barrier for an R domain growing from an AR state ($\Delta_0 = 2\,a$, $\kappa = 3\,a^{-2}k_{\mathrm{B}}T$). The arrowed line shows $J/B = 8$, as used in Fig. 6.

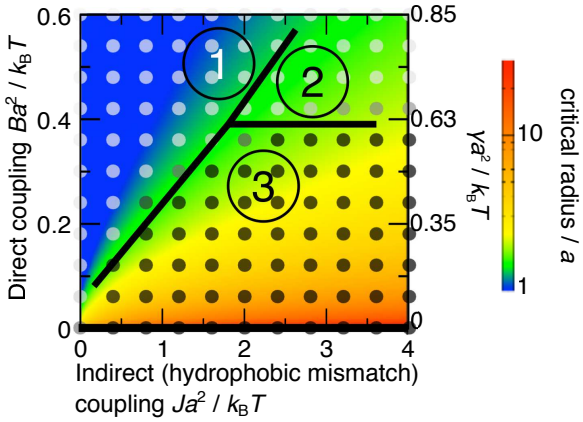

FIG. 8. As Fig. 7 but showing the calculated critical radius for registered domain nucleation.

D. Nucleation barrier and critical radius landscapes

Fig. 6 (inset) implies that increasing J for a fixed ratio J/B and fixed κ (equivalently, increasing ξ) first increases then reduces the nucleation barrier. In the limit of large κ one would expect increasing J and B to simply increase the energy scale, hence the nucleation barrier. But when J is comparable to κ, the mechanism illustrated in Fig. 5b takes over; increasing $\xi \equiv \sqrt{2\tilde{J}a^2/\kappa}$ reduces the effective thickness mismatch for small nuclei, thus reducing the hydrophobicity penalty for nucleation and reducing the nucleation barrier.

The nucleation theory can be related to the simulations by plotting landscapes of the nucleation barrier $\Delta G(R^*)$ (Fig. 7) and critical radius R^* (Fig. 8). A small barrier clearly facilitates nucleation, although the role of the critical radius is more subtle [23–25]. However, one important factor is that for smaller critical radii, regions randomly enriched in registration from the initial quench are more likely to be near or above the critical radius, so can grow more easily.

The predicted energetics for nucleation are consistent with the classes of kinetics identified in Fig. 2. Where the R instability mode is fastest, nucleation energetics are irrelevant since the equilibrium phases are formed immediately. If the AR mode is fastest, a successful subsequent transition to equilibrium R-R coexistence generally occurs where the predicted nucleation barrier and critical radius are smaller.

V. DISCUSSION

In this paper we have studied phase-separation kinetics in a bilayer subject to competing registered (R) and antiregistered (AR) instabilities. We have modelled the nucleation of R domains in the case where the initial spinodal instability leads to a metastable AR state.

If the fastest-growing instability mode is R, spinodal decomposition directly into the equilibrium registered phases takes place (class 1 Fig. 2). If the AR mode grows fastest then a metastable AR state forms, and nucleation is required to reach equilibrium registration (class 2 Fig. 2). Unsuccessful nucleation leaves the bilayer metastably stuck indefinitely (class 3 Fig. 2).

The key parameters for the nucleation energetics are the indirect inter-leaflet coupling J via hydrophobic mismatch (favouring antiregistration), and the direct coupling B which favours registration. Both of these parameters couple to the stiffness κ, which determines how easily mixed amphiphiles can change their tail length and ordering to adapt to one another's presence [1]. Here we have focused on an equimolar mixture in both leaflets such that AR-AR coexistence competes with R-R; the kinetic considerations are qualitatively similar for other overall compositions, in which other states including three-phase coexistence (AR-AR-R or R-R-AR) can enter [2].

Nucleation implies a critical radius, which a registered domain must exceed so that the penalty of thickness mismatch at the perimeter does not outweigh the bulk free energy gain of registration. This does not mean that domains "automatically" register once they exceed a certain size, as could be inferred from Refs. [5, 26]; if nucleation of registered domains is prohibitive, then metastably trapped antiregistered domains could become arbitrarily large. By examining the effect of thickness mismatch at the boundary of a nucleating registered domain, we showed that the process departs strongly from classical nucleation theory due to deformation of the thickness profile, which reduces the effective line tension of small nuclei. For small nuclei, the deformation essentially spreads over the whole nucleus, reducing the effective hydrophobic mismatch. This prediction is supported by recent molecular simulation of coarsening of a quenched bilayer [22], where registered liquid-ordered and liquid-disordered domains became respectively thicker and thinner as they grew through time.

The phase equilibria of "macroscopic" domains (which coarsen until limited by bilayer size) are not influenced by edge energies and, for most reasonable parameters, we predict that registration is the equilibrium state in bulk [1, 2], as seen in fluorescence studies of large domains [27, 28]. At the opposite end of the size spectrum, experiments reveal pairwise antiregistration at the single-amphiphile level [10, 29], as also reported in simulation [8] and predicted by our mean-field theory [1]. In between these size regimes, edge energies can influence the equilibrium state; for example, the antiregistered domains in Ref. [9] are probably metastable in the limit of large size but could be stabilised if the simulation box is too small to accommodate a supercritical registered domain.

This has important physical consequences, because cell membrane rafts or clusters are not macroscopic. Whether the small domain size *in vivo* is due to elastic repulsion

[30], hybrid lipids [31], critical fluctuations [32], active recycling [33, 34] or another mechanism, it is crucial to recognise that edge energies could influence the thermodynamic preference and even stabilise antiregistration. Although the cell membrane is maintained out of equilibrium, thermodynamic driving forces can still be expected to play an important role. The potential importance of this size-dependence is underlined by the fact that our estimated critical radii (Fig. 8) can be of the order of putative lipid raft sizes [35], although we have used a relatively large thickness mismatch. The basic biophysical question is; if a cluster of longer lipids and proteins exists in one leaflet, does it co-localise a similar cluster in the opposite leaflet to maintain transbilayer structural similarity, or does it choose shorter lipids and proteins to maintain uniform thickness? Our work implies that finite-size effects, metastable states and phase-transition kinetics may be key in determining the answer.

Appendix A: Calculations for continuum theory

In our nucleation theory the response of the actual profiles $\ell^{\mathrm{t,b}}(r)$ to variations in the ideal thicknesses $\ell_0^{\mathrm{t,b}}(r)$ is calculated as follows. Varying G_{cont} (Eq. 5) with respect to ℓ^{t} and ℓ^{b} results in a pair of differential equations that can be combined to yield independent equations for the thickness difference $\Delta(r) \equiv \ell^{\mathrm{t}}(r) - \ell^{\mathrm{b}}(r)$ and the total $d(r)$

$$\kappa\left(\Delta(r) - \Delta_0^*(r)\right) + 2B\Delta(r) = 0 \ , \tag{A1a}$$

$$r\kappa\left(d_0^*(r) - d(r)\right) + 2\tilde{J}a^2\frac{d}{dr}\left(r\frac{dd(r)}{dr}\right) = 0 \ . \tag{A1b}$$

In the above we have used the ideal thickness difference and total profiles, $\Delta_0^*(r) \equiv \ell_0^{\mathrm{t}}(r) - \ell_0^{\mathrm{b}}(r)$ and $d_0^*(r) \equiv \ell_0^{\mathrm{t}}(r) + \ell_0^{\mathrm{b}}(r)$.

In the AR background the S and U species' lengths are not equal to their ideal values – the direct coupling B encourages equality of amphiphile length (thus degree of ordering) across the bilayer. Eq. A1a is solved by

$$\Delta(r) = \frac{\kappa\Delta_0^*(r)}{\kappa + 2B} \ . \tag{A2}$$

Inserting Eq. 6 for the ideal thicknesses yields Eq. 7. The total thickness before the nucleus is introduced is uniform (Eq. 9).

After introducing the R nucleus, the difference in ideal thicknesses is zero within the R nucleus ($\Delta_0^*(r) = 0$ for $r \leq R$), which gives Eq. 11. The total thickness profile is found by solving Eq. A1b (which is expressible as a modified Bessel's equation of order zero). We require that the gradient vanishes at the centre of the nucleus ($d\,d(r)/dr|_{r=0} = 0$), and that the total thickness approaches its ideal value away from the domain ($d(\infty) = \ell_{S0} + \ell_{U0} = d_0$). The profile $d(r)$ and its gradient are required to be continuous at $r = R$ in order to match the profiles inside and outside the nucleus. With ideal thicknesses given by Eq. 10, this yields Eq. 12.

To calculate the energy ΔG required to introduce the registered nucleus, we consider the initial energy $G_{\mathrm{cont}}^{\mathrm{AR}}$ from inserting Eqs. 7 and 9 into Eq. 5, and the energy $G_{\mathrm{cont}}^{\mathrm{nuc.}}$ when the nucleus is introduced, from inserting Eqs. 11 and 12 instead. The energy for introducing the nucleus is then

$$\Delta G = G_{\mathrm{cont}}^{\mathrm{nuc.}} - G_{\mathrm{cont}}^{\mathrm{AR}} \ . \tag{A3}$$

Since Eqs. 11 and 12 split at the nucleus boundary $r = R$, we evaluate separate contributions to ΔG outside and inside the nucleus and find

$$\Delta G^{\mathrm{out}} = \int_R^\infty \frac{2\pi r dr}{a^2}\left(\frac{\tilde{J}a^2}{2}\left(\frac{d}{dr}d^{\mathrm{nuc.}}(r)\right)^2 + \frac{\kappa}{4}\left(d^{\mathrm{nuc.}}(r) - d_0\right)^2\right) \ , \tag{A4}$$

$$\Delta G^{\mathrm{in}} = \int_0^R \frac{2\pi r dr}{a^2}\left(\frac{\tilde{J}a^2}{2}\left(\frac{d}{dr}d^{\mathrm{nuc.}}(r)\right)^2 + \frac{\kappa}{4}\left(d^{\mathrm{nuc.}}(r) - 2\ell_{S0}\right)^2 - \frac{\Delta_0^2\kappa B}{2(\kappa + 2B)}\right) \ , \tag{A5}$$

ΔG^{out} contains only positive contributions, resulting from deformation of the total thickness profile by the nucleus. ΔG^{in} contains similar deformation terms, but also a negative term resulting from the fact that there is now no inter-leaflet mismatch in the region $r \leq R$. The sum $\Delta G^{\mathrm{in}} + \Delta G^{\mathrm{out}}$ leads to Eq. 16.

Note that the negative term in ΔG^{in} is precisely the estimated inter-leaflet mismatch energy density γ under our microscopic definition [1]. Near the strong-segregation regime this is a close approximation to the difference in bulk free-energy density between registered and antiregistered phases (which can be used to construct an alternative "macroscopic" definition of γ [1]), becoming exact in the strong-segregation limit assumed here. However, in principle one could replace this term with the actual free-energy difference in cases where the correspondence between microscopic and macroscopic γ breaks down [1].

ACKNOWLEDGMENTS

We acknowledge discussions with members of the EPSRC CAPITALS programme grant. This work was initiated at the University of Leeds, Leeds, United Kingdom, and was funded by EPSRC grant EP/J017566/1 and by Georgetown University. PDO gratefully acknowledges the support of the Ives endowment.

1. Williamson, J. J., and P. D. Olmsted, 2015. Registered and Antiregistered Phase Separation of Mixed Amphiphilic Bilayers. *Biophys. J.* 108:1963–1976.
2. Williamson, J. J., and P. D. Olmsted, 2015. Ostwald's rule of stages in phase-transition kinetics of coupled bilayer leaflets. ArXiv:1505.02078.
3. Garbès Putzel, G., and M. Schick, 2008. Phase Behavior of a Model Bilayer Membrane with Coupled Leaves. *Biophys. J.* 94:869–877.
4. Garbès Putzel, G., M. J. Uline, I. Szleifer, and M. Schick, 2011. Interleaflet Coupling and Domain Registry in Phase-Separated Lipid Bilayers. *Biophys. J.* 100:996–1004.
5. May, S., 2009. Trans-monolayer coupling of fluid domains in lipid bilayers. *Soft Matter* 5:3148–3156.
6. Collins, M. D., and S. L. Keller, 2008. Tuning lipid mixtures to induce or suppress domain formation across leaflets of unsupported asymmetric bilayers. *Proc. Natl. Acad. Sci.* 105:124–128.
7. Risselada, H. J., and S. J. Marrink, 2008. The molecular face of lipid rafts in model membranes. *Proc. Natl. Acad. Sci.* 105:17367–17372.
8. Stevens, M. J., 2005. Complementary Matching in Domain Formation within Lipid Bilayers. *J. Am. Chem. Soc.* 127:15330–15331.
9. Perlmutter, J. D., and J. N. Sachs, 2011. Interleaflet Interaction and Asymmetry in Phase Separated Lipid Bilayers: Molecular Dynamics Simulations. *J. Am. Chem. Soc.* 133:6563–6577.
10. Zhang, J., B. Jing, N. Tokutake, and S. L. Regen, 2004. Transbilayer Complementarity of Phospholipids. A Look beyond the Fluid Mosaic Model. *J. Am. Chem. Soc.* 126:10856–10857.
11. Ostwald, W., 1897. Studien über die Bildung und Umwandlung fester Körper. *Z. Phys. Chem.* 22:289–330.
12. In a real system in which amphiphile species' molecular areas may differ, $(0.5, 0.5)$ refers instead to an equal area fractions mixture in each leaflet [2].
13. Stukowski, A., 2010. Visualization and analysis of atomistic simulation data with OVITO the Open Visualization Tool. *Modelling Simul. Mater. Sci. Eng.* 18:015012.
14. Komura, S., H. Shirotori, P. D. Olmsted, and D. Andelman, 2004. Lateral phase separation in mixtures of lipids and cholesterol. *Europhys. Lett.* 67:321.
15. Wallace, E. J., 2005. Influence of microstructure on the phase behaviour of lipid membranes. Ph.D. thesis, University of Leeds.
16. Needham, D., and R. Nunn, 1990. Elastic deformation and failure of lipid bilayer membranes containing cholesterol. *Biophys. J.* 58:997 – 1009.
17. Rawicz, W., K. Olbrich, T. McIntosh, D. Needham, and E. Evans, 2000. Effect of Chain Length and Unsaturation on Elasticity of Lipid Bilayers. *Biophys. J.* 79:328 – 339.
18. García-Sáez, A. J., S. Chiantia, and P. Schwille, 2007. Effect of Line Tension on the Lateral Organization of Lipid Membranes. *J. Biol. Chem.* 282:33537–33544.
19. Lin, W.-C., C. D. Blanchette, T. V. Ratto, and M. L. Longo, 2006. Lipid Asymmetry in DLPC/DSPC-Supported Lipid Bilayers: A Combined AFM and Fluorescence Microscopy Study. *Biophys. J.* 90:228 – 237.
20. Huang, K., 1987. Statistical Mechanics. Wiley, New York.
21. Bleecker, J. V., P. A. Cox, and S. L. Keller. Comparing Lo/Ld Membrane Thickness Mismatch and Miscibility Transition Temperatures using Fluorescence and Atomic Force Microscopy. *Biophys. J.* 108:241a–.
22. Jefferys, E., M. S. P. Sansom, and P. W. Fowler, 2014. NRas slows the rate at which a model lipid bilayer phase separates. *Faraday Discuss.* 169:209–223.
23. Ryu, S., and W. Cai, 2010. Numerical tests of nucleation theories for the Ising models. *Phys. Rev. E* 82:011603.
24. Vehkamäki, H., 2006. Classical Nucleation Theory in Multicomponent Systems. Springer-Verlag.
25. Vehkamäki, H., A. Määttänen, A. Lauri, I. Napari, and M. Kulmala, 2007. Technical Note: The heterogeneous Zeldovich factor. *Atmos. Chem. Phys.* 7:309–313.
26. Wallace, E. J., N. M. Hooper, and P. D. Olmsted, 2006. Effect of Hydrophobic Mismatch on Phase Behavior of Lipid Membranes. *Biophys. J.* 90:4104–4118.
27. Korlach, J., P. Schwille, W. W. Webb, and G. W. Feigenson, 1999. Characterization of lipid bilayer phases by confocal microscopy and fluorescence correlation spectroscopy. *Proc. Natl. Acad. Sci.* 96:8461–8466.
28. Dietrich, C., L. Bagatolli, Z. Volovyk, N. Thompson, M. Levi, K. Jacobson, and E. Gratton, 2001. Lipid Rafts Reconstituted in Model Membranes. *Biophys. J.* 80:1417–1428.
29. Zhang, J., B. Jing, V. Janout, and S. L. Regen, 2007. Detecting Cross Talk between Two Halves of a Phospholipid Bilayer. *Langmuir* 23:8709–8712.
30. Meinhardt, S., R. L. C. Vink, and F. Schmid, 2013. Monolayer curvature stabilizes nanoscale raft domains in mixed lipid bilayers. *Proc. Nat. Acad. Sci.* 110:4476–4481.
31. Palmieri, B., T. Yamamoto, R. C. Brewster, and S. A. Safran, 2014. Line active molecules promote inhomogeneous structures in membranes: Theory, simulations and experiments. *Adv. Colloid Interface Sci.* 208:58 – 65.
32. Veatch, S. L., O. Soubias, S. L. Keller, and K. Gawrisch, 2007. Critical fluctuations in domain-forming lipid mixtures. *Proc. Natl. Acad. Sci.* 104:17650–17655.
33. Fan, J., M. Sammalkorpi, and M. Haataja, 2008. Domain Formation in the Plasma Membrane: Roles of Nonequilibrium Lipid Transport and Membrane Proteins. *Phys. Rev. Lett.* 100:178102.
34. Turner, M. S., P. Sens, and N. D. Socci, 2005. Nonequilibrium Raftlike Membrane Domains under Continuous Recycling. *Phys. Rev. Lett.* 95:168301.
35. Lingwood, D., and K. Simons, 2010. Lipid Rafts As a Membrane-Organizing Principle. *Science* 327:46–50.